DESIGN OF THE CLIC MAIN LINAC ACCELERATING STRUCTURE FOR CLIC CONCEPTUAL DESIGN REPORT

A. Grudiev, W. Wuensch, CERN, Geneva, Switzerland

Abstract

The design of the CLIC main linac accelerating structure has been refined based on an improved understanding of the high-gradient limits given by rf breakdown and pulsed surface heating. In addition, compact couplers have been developed and HOM damping loads have been designed. The rf design has also been made consistent with details of the present manufacturing procedure, based on bonded asymmetrical disks, and with requirements coming from integration of the accelerating structure in the two-beam module [1]. This completion and refinement of the structure design has been made to produce the self-consistent parameter set required for preparation of the CLIC conceptual design report (CDR).

RF DESIGN

Over the past few years, there has been significant progress in demonstrating the feasibility of accelerating structures operating at 100 MV/m [2]. Very recently tests have also shown that structures with damping features can reach within 80 to 90% of the gradients of undamped structures [3]. Based on these results, a program to further improve the rf design and incorporate further features has been made. In this report the modification and further development of the rf design of the CLIC main linac accelerating structure [4] is described.

Basic Cell Geometry and HOM Damping

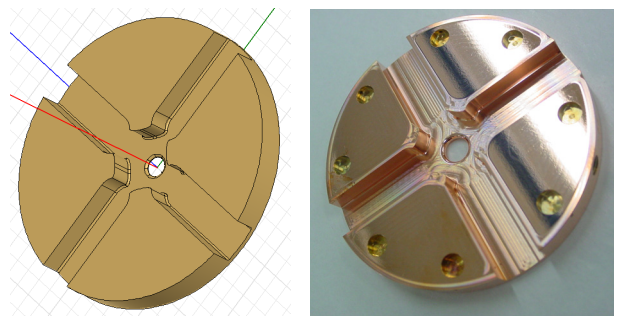

Figure 1: Basic cell geometry of the accelerating structure with strong waveguide HOM damping is shown. 3D model (left) and copper piece (right).

The basic cell geometry is shown in Fig. 1. It is very similar to the geometry described in [4] but with several differences. First, the cell geometry is adapted to the manufacturing process based on the bonding of disks with one side being flat and the other side carrying all the cell features. This is the facing side in Fig. 1. The previous design [4] was based on quadrant technology and had doubly rounded cells. Second, the geometry of the outer wall and damping waveguides have been optimized to minimize both the pulsed surface heating temperature rise on the outer wall and the penetration distance of the fundamental mode into the damping waveguides while maintaining the same damping efficiency. This has been achieved through reducing both the aperture to the damping waveguide and the damping waveguide width. The smaller penetration distance allows a smaller overall transverse size since the HOM damping loads made of SiC can be placed closer to the axis without affecting the Q-factor of the fundamental mode. In the presented design the distance from the axis of the structure to the tip of SiC damping load is 50 mm. The geometry of the load placed in the damping waveguide is shown in Fig. 2. It has 30 mm long part which is tapered from 1x1 mm cross-section to 5x5 mm over 30mm and a 10 mm long part of the latter cross-section.

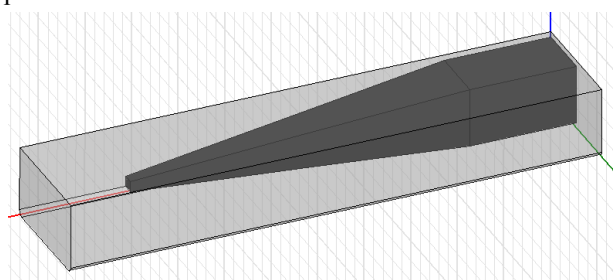

Figure 2: Internal volume of a damping waveguide equipped with HOM load made of SiC is shown.

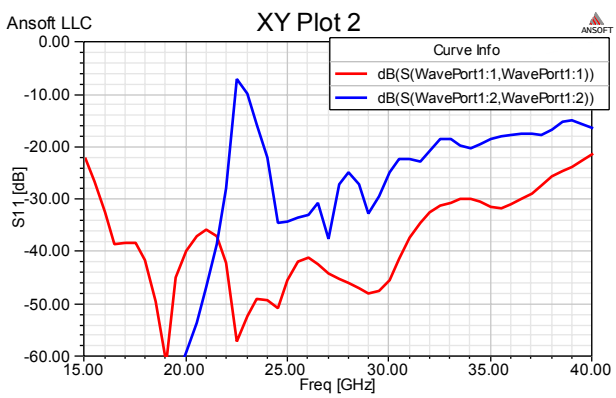

Figure 3: Reflections from SiC load in the damping waveguide are shown both for TE10 (red) and for TE01 (blue) modes.

This setup provides very broad band absorption of the wakefields and is used to terminate each damping waveguides of the structure. The reflections of the TE10 and TE01 modes from the load are calculated using HFSS frequency domain code [5] assuming parameters of the SiC material as it was measured in [6] ($\varepsilon' = 13$, $\tan\delta = 0.16$). The geometry of the load has been optimized to keep the reflections below -30 dB for TE10 mode and

below -20 dB for TE01 mode. The final results are presented in Fig. 3. These reflections do not compromise the HOM damping performance primarily determined by the cell to damping waveguide coupling.

Tapering and Couplers

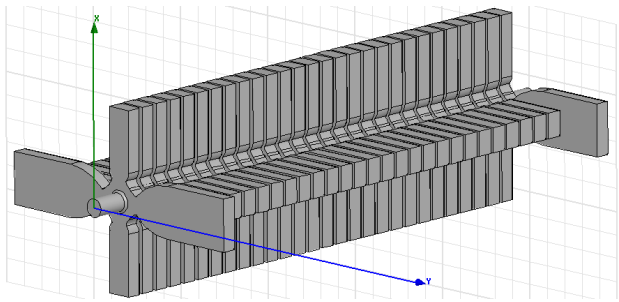

Figure 4: Internal volume of the full structure is shown.

The internal volume geometry of the full structure is shown in Fig. 4. The iris range was kept the same as in [4] but the tapering is now over 26 rather than 24 cells. The reason for the change of the number of regular cells is a new, more compact than assumed in [4] design of the input and output coupler cells which is shown in Fig. 5. The coupling is magnetic but the coupler cell geometry is quite different from that traditionally used and resembles very much the regular cell geometry. The only difference is that in the coupler cell, two opposite waveguides are of the standard WR-90 width forming a double-feed coupler cell. The other two damping waveguides are kept in place to maintain the damping as efficient as in the regular cells. Furthermore, it naturally minimizes the quadrupolar kick, since the geometry is close to the regular cell geometry where the quadrupolar kick is canceled by the symmetry. The coupler provides about the same acceleration as a regular cell and both surface magnetic and electric fields do not exceed maximum values in the rest of the structure. As a double-feed coupler it must be fed in phase from both sides. In the case of a magic-T, the wakefields coming in opposite direction from the coupler cell into the power waveguides are out of phase for the TE10 mode and in phase for TE01 mode. Under these conditions both modes are guided to the 4th arm of the magic-T which is terminated by a load. This provides efficient HOM damping in both planes in the couplers cells which is not negligible part of the full structure.

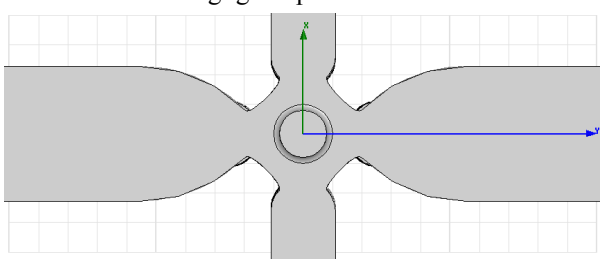

Figure 5: Internal volume of the coupler cell.

The updated parameter list for the modified structure is presented in Table 1. Several small differences (at the level of few percent) are to be highlighted: lower Q-factor and shunt impedance, lower group velocity and two more cells increase slightly filling time and decrease input power required for 100 MV/m average loaded accelerating gradient, slightly lower surface electric field and last but not least pulse surface heating temperature rise which was reduced by 11 % from 53 K [4] to 47 K.

Table 1: Updated Structure Parameters

Average loaded accelerating gradient	100 MV/m
Frequency	12 GHz
RF phase advance per cell	2π/3 rad.
Average iris radius to wavelength ratio	0.11
Input, Output iris radii	3.15, 2.35 mm
Input, Output iris thickness	1.67, 1.00 mm
Input, Output group velocity	1.65, 0.83 % of c
First and last cell Q-factor (Cu)	5536, 5738
First and last cell shunt impedance	81, 103 MΩ/m
Number of regular cells	26
Structure length including couplers	230 mm (active)
Bunch spacing	0.5 ns
Bunch population	3.7×10^9
Number of bunches in the train	312
Filling time	67 ns
Total pulse length	242 ns
Peak input power	61.3 MW
RF-to-beam efficiency	27.7 %
Maximum surface electric field	230 MV/m
Maximum pulsed surface heating temperature rise	47 K

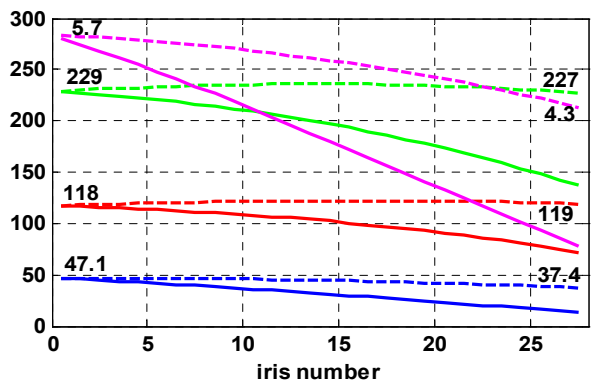

Figure 6: The fundamental mode properties are shown. The traces from top to bottom are: S_c·40 [W/μm^2](pink), surface electric field [MV/m](green), accelerating gradient [MV/m](red), pulse surface temperature rise [K](blue). Dashed traces are unloaded and solid are beam loaded conditions.

Both the iris radius and thickness are tapered linearly in order to provide an optimum distribution of various high-power parameters and to avoid the hot spots along the structure. Distributions of these parameters are shown in Fig. 6. The unloaded structure gradient, the surface electric field rise and the temperature rise are made to be constant. In Fig. 6, the pink line shows the distribution of a new field quantity S_c [7] which serves as a limit for high gradient performance and to certain extent combines both the power and the surface electric field constraints.

Wakefields

Table 2: Parameters of the lowest dipole-band modes

Cell	First	Middle	Last
Q-factor	11.1	8.7	7.1
Amplitude [V/pC/mm/m]	125	156	182
Frequency [GHz]	16.91	17.35	17.80

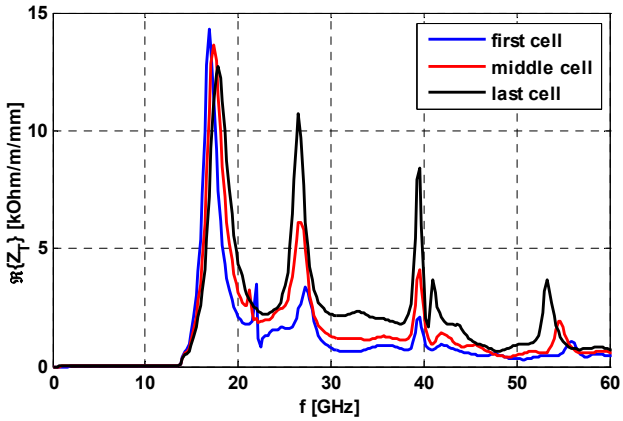

Figure 7: Transverse impedances of the first (blue), middle (red) and last (black) cells.

The tapering also provides detuning of the higher order modes which is an important effect even for heavily damped structures. The relative contributions of the heavy damping and detuning to the transverse wakefields spectrum are illustrated in Fig. 7. Parameters of the lowest dipole-band modes calculated from the fitting to the impedance curves are listed in Table 2. The transverse wake of the full structure was computed in time domain using parallel code GdfidL [8]. The results for both planes are shown in Fig 8. The difference between two planes comes only from the coupler cells and is very small. One can see that both wakes at the position of the second bunch which is 0.15 m are below the 7 V/pC/mm/m, as required for beam dynamics.

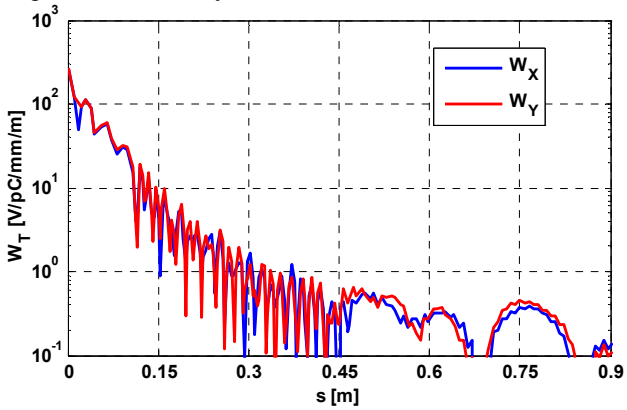

Figure 8: The envelope of the transverse wakefields for both planes is shown. The CLIC bunch spacing is 0.15 m.

CONCLUSIONS

The design of the CLIC main linac accelerating structure has been refined and completed taking into account the manufacturing and integration constraints and at the same time maintaining the same or better rf performance. It has allowed producing a self-consistent parameter set required for preparation of the CLIC CDR.

REFERENCES

[1] G. Riddone, et al., "Two beam module design and integration", these proceedings.
[2] T. Higo et. al., "Advances in X-band TW Accelerator Structures Operating in the 100 MV/m Regime," Proc. IPAC10, Kyoto, Japan.
[3] S. Doebert et. al.., "First High-Power Tests of CLIC Prototype Accelerating Structures with HOM Waveguide Damping", these proceedings.
[4] A. Grudiev, W. Wuensch, "Design of X-band accelerating structure for the CLIC main linac", LINAC'08, Victoria BC, Canada, 2008.
[5] Ansoft HFSS, www.Ansoft.com.
[6] M. Luong, I. Wilson, W. Wuensch, "RF Loads for the CLIC Multibunch Structure", PAC'99, New York, 1999.
[7] A. Grudiev, S. Calatroni, and W. Wuensch, "New local field quantity describing the high gradient limit of accelerating structures", Phys. Rev. ST Accel. Beams 12, 102001 (2009).
[8] W. Bruns, www.gdfidl.de.